Influence of heterogeneous thermal conductivity on the long-term evolution of the lower mantle thermochemical structure: implications for primordial reservoirs

Joshua M. Guerrero[1], Frédéric Deschamps[1], Yang Li[2], Wen-Pin Hsieh[1], and Paul J. Tackley[3]

[1]Institute of Earth Sciences, Academia Sinica, Taipei, Taiwan
[2]State Key Laboratory of Lithospheric Evolution, Institute of Geology and Geophysics, Institutions of Earth Science, Chinese Academy of Sciences, Beijing, China
[3]Department of Earth Sciences, ETH Zürich, Zürich, Switzerland

Correspondence: Joshua Martin Guerrero (joshua@earth.sinica.edu.tw), Frédéric Deschamps (frederic@earth.sinica.edu.tw)

Abstract. The long-term evolution of the mantle is simulated using 2D spherical annulus geometry to examine the effect of heterogeneous thermal conductivity on the stability of reservoirs of primordial material. Often in numerical models, purely depth-dependent profiles emulate mantle conductivity (taking on values between 3 and 9 $\mathrm{Wm^{-1}K^{-1}}$). This approach synthesizes the mean conductivities of mantle materials at their respective conditions in-situ. However, because conductivity also

5 depends on temperature and composition, the effects of these dependencies on mantle conductivity are masked. This issue is significant because dynamically evolving temperature and composition introduce lateral variations in conductivity, especially in the deep mantle. Minimum and maximum variations in conductivity are due to the temperatures of plumes and slabs, respectively, and depth- dependence directly controls the amplitude of conductivity (and its variations) across the mantle depth. Our simulations allow assessing the consequences of these variations on mantle dynamics, in combination with the reduction of

10 thermochemical pile conductivity due to its expected high temperatures and enrichment in iron, which has so far not been well examined. The mean conductivity ratio from bottom-to-top indicates the relative competition between the decreasing effect with increasing temperature and the increasing effect with increasing depth. We find that, when depth- dependence is stronger than temperature- dependence, a mean conductivity ratio > 2 will result in long-lived primordial reservoirs. Specifically, for the mean conductivity profile to be comparable to the conductivity often assumed in numerical models, the depth- dependent

15 ratio must be at least 9. When conductivity is underestimated, the imparted thermal buoyancy (from heat-producing element enrichment) destabilizes the reservoirs and influences core-mantle boundary coverage configuration and the onset of dense material entrainment. The composition- dependence of conductivity only plays a minor role that behaves similarly to a small conductivity reduction due to temperature. Nevertheless, this effect may be amplified when depth- dependence is increased. For the cases we examine, when the lowermost mantle's mean conductivity is greater than twice the surface conductivity, reservoirs

20 can remain stable for very long periods of time, comparable to the age of the Earth.

1 Introduction

Tomographic studies of Earth's lower mantle reveal the presence of two large low-velocity provinces (LLVPs) that overlie the core-mantle boundary (CMB). Located below the Pacific Ocean and Africa, LLVPs have a combined coverage of up to 30% of the CMB with vertical extents as high as 1200 km (Garnero et al., 2016). Detailed LLVP structure remains uncertain. In partic-
ular, spectral elements waveform tomographic models (e.g., French & Romanowicz, 2014), which achieve higher resolution, suggest a plume-bundle morphology with a potential dense basal layer (e.g., Davaille & Romanowicz, 2020) whereas models based on travel times only suggest tall dense dome-like piles (e.g., Houser et al., 2008). Independently of the exact geometry of LLVPs, authors define these anomalous regions either as purely thermal (Davies et al., 2012) or thermochemical (e.g., Trampert et al., 2004) in nature. However, several important observations, including the anti-correlation between shear and bulk-sound
velocities, are better explained if they are not purely thermal in origin (Deschamps et al., 2015). LLVPs (or piles) may further affect plume generation (e.g., Tan et al., 2011; Heyn et al., 2020) and core-to-mantle heat flow (e.g., Deschamps & Hsieh, 2019). Furthermore, plumes sourced from deep mantle reservoirs may provide a mechanism to explain the diverse chemistry observed in ocean island basalts (Deschamps et al., 2011). Two end-member views on the origin of piles (and their chemical composition) have been proposed: a primordial layer (composed of anomalously dense material) (e.g., Labrosse et al., 2007;
Lee et al., 2010); and a growing layer (composed of mid-ocean ridge basalt sinking in the deep mantle and accumulating at the CMB) (e.g., Hirose et al., 1999; Nakagawa et al., 2009). However, mantle convection likely modifies the composition of piles over time and sources for the chemistry observed at the surface may be difficult to trace.

Piles' unique chemical composition determines physical properties, most importantly density, viscosity, and enrichment in HPEs that affect their long-term stability. These property values remain uncertain, but numerical simulations that emulate
Earth-like piles help constrain their ranges (e.g., Li et al., 2014, 2018, 2019; Gülcher et al., 2020; Citron et a., 2020). An important property, thermal conductivity, often radially parametrized, controls the heat flow between piles and the surrounding mantle and hence mean pile temperature (i.e., thermal buoyancy). Because thermal conductivity can vary significantly with temperature, pressure, and composition, heterogeneous heat transfer in the lowermost mantle can strongly affect the long-term stability of piles. The evolution and stability of piles will differ between radial and fully heterogeneous conductivity models.
Measured and estimated thermal conductivities of minerals are determined at variable temperature and pressure conditions relevant to regions of the mantle at shallow and great depths. In addition, aggregate compositions with variable fractions of mineral concentrations and elemental inclusions influence the mantle conductivities at depth. Thus, studies that investigate pressure effects (at fixed temperature) (e.g., Ohta et al., 2012; Dalton et al., 2013; Goncharov et al., 2015; Hsieh et al., 2017, 2018) or thermal effects (at fixed pressure) (e.g., Kanamori et al., 1968; Katsura, 1997; Hofmeister, 1999; Manthilake et
al., 2011; Zhang et al., 2019) often include measurements on mineral samples with additional elemental impurities. Compared to pure magnesium end-members of mantle minerals, inclusion of other elements (e.g., iron or aluminium), into an aggregate sample can reduce thermal conductivity substantially (e.g., Ohta et al., 2012; Hsieh et al., 2017, 2018). Enrichment of a mantle aggregate in iron or aluminium-bearing minerals greatly reduces its total conductivity, as might be the case for LLVPs (Deschamps & Hsieh, 2019). In numerical models, this effect can be emulated by parametrizing a percentage reduction with the

55 primordial composition field. Li et al. (2022) showed that composition- dependence of conductivity can raise the topography of thermochemical piles.

Estimates of thermal conductivity at high temperature and high pressure are available, but, Geballe et al. (2020) point out that calculations of thermal conductivity for bridgmanite, for example, can differ by a factor of 10 between different studies (Haigis et al., 2012; Dekura et al., 2013; Ammann et al., 2014; Tang et al., 2014; Stackhouse et al., 2015). In addition, labo-

60 ratory measurements for pyrolite at both high temperature and pressure are still relatively unconstrained and coarsely sampled (e.g., $5.9^{+4.0}_{-2.3}$ $\mathrm{Wm^{-1}K^{-1}}$ at 124 GPa and 2000 to 3000 K (Geballe et al., 2020)).

In general, measurements from mantle minerals show that thermal conductivity increases with increasing pressure. At a fixed temperature (e.g., at room temperature $\sim 300K$), measurements of thermal conductivity increase with an approximately linear trend. At greater temperatures, conductivity decreases, but (even with temperature corrections for adiabaticity) the linear

65 increase in conductivity with pressure is maintained. Enrichment of bridgmanite and ferropericlase (lower mantle minerals) in iron significantly reduces the zero- pressure reference value and the slope of thermal conductivity (e.g., Deschamps & Hsieh, 2019). For iron-bearing bridgmanite and ferropericlase at room temperature and CMB pressures, thermal conductivities fall between 10 and 35 $\mathrm{Wm^{-1}K^{-1}}$ and between 35 and 60 $\mathrm{Wm^{-1}K^{-1}}$, respectively (Deschamps & Hsieh, 2019). Considering thermal conductivities in this range for the lowermost mantle, we expect that heat exchange in that region will be more efficient.

70 However, this effect will be curbed by temperature dependence.

The thermal conductivity decreases with increasing temperature and follows a relationship proportional to T^{-n}. The mechanism controlling lattice heat transport determines the exponent n and the strength of temperature dependence. Experimental data (e.g., Klemens, 1960; Xu et al., 2004; Dalton et al., 2013) suggest that n is typically between 0.5 for (Fe, Al)-bearing minerals (three-phonon scattering at low phonon frequency) and 1.0 for $MgSiO_3$ (anharmonic three-phonon scattering). Values

75 below $n = 0.5$ are possible, suggesting mantle minerals may be weakly temperature-dependent. Alternative thermal conductivity parametrization can lead to different n values. For instance, with additional temperature dependences, Hofmeister (1999) finds $n = 0.33$ for silicates and 0.9 for MgO. Under upper mantle conditions and density dependence, (Manthilake et al., 2011) finds that $n \sim 0.2$ for Fe-bearing bridgmanite and periclase. For a typical temperature dependence ($n = 0.5$) and a reference temperature of 300 K, a lowermost mantle temperature of 3000 K results in a $\sim 70\%$ reduction in conductivity. Therefore, at

80 lowermost mantle pressures, a lowermost mantle conductivity of 7.5 W/m/K at 3000 K corresponds to a conductivity measurement of 25 $\mathrm{Wm^{-1}K^{-1}}$ a room-temperature. Thus, the effect of temperature plays a significant role in making the lowermost mantle very poor at transferring heat.

Temperature and depth variations in conductivity had been considered previously for Boussinesq or extended Boussinesq fluid simulations. Using Hofmeister (1999)'s lattice conductivity formulation in an isoviscous Boussinesq fluid, several effects

85 were observed: temperature increases in the lower mantle (Dubuffet et al., 1999), a stabilizing effect on mantle flow, which manifests in thick and stable plumes (Dubuffet & Yuen, 2000), and the rapid thermal assimilation of cold downwelling slabs (Dubuffet et al., 2000). Yanagawa et al. (2005) examined the effects of a purely temperature dependent conductivity in conjunction with a strongly temperature dependent viscosity and observed a cooler, thinner, upper thermal boundary layer when compared to a constant conductivity. More recently, Tosi et al. (2013) parametrized a temperature and pressure dependent

thermal conductivity (and thermal expansivity) derived from mineral physics data. They observed a strong increase in bulk mantle temperature, which suppresses bottom thermal boundary layer instabilities and causes mantle flow to be driven by instabilities at the upper thermal boundary. Li et al. (2022) examined the effect of thermal conductivity in simulations featuring a compressible fluid and thermochemical piles, but conductivity changes with temperature were not included. In addition to lateral variations in temperature related to the flow, a compressible fluid introduces an adiabatic temperature increase with depth. For an adiabatic temperature gradients in the lower mantle between 0.2 to 0.4 Kkm^{-1}, temperature will increase by approximately 600 K from the 660-transition to the core-mantle boundary (Katsura, 2022). Given the strength of thermal conductivity's dependence on temperature, such an adiabatic temperature increase in the lowermost mantle cannot be neglected in primordial reservoir's total conductivity. Neglecting compressibility may result in an overestimation of thermal conductivity, thus, changing the dynamics and evolution of primordial reservoirs.

In this study, we use compressible thermochemical mantle convection models to examine the effect of temperature-, depth-, and composition- dependent conductivity on the stability of thermochemical piles. By refining the conductivity parameters controlling the bottom-to-top conductivity ratio, we try to reproduce conductivity values comparable to lower mantle measurements. Furthermore, we determine the longevity of systems evolving with Earth-like primordial reservoirs. First, we isolate the effect of purely depth- dependent thermal conductivity to understand the dynamics of primordial reservoirs under different lowermost mantle conductivity conditions. Next, we introduce the effect of temperature- and composition- dependence to examine how the heating conditions in conjunction with depth- dependence affect pile evolution. We conclude by examining the effect of a fully heterogeneous conductivity (featuring depth- dependence based on mantle minerals) on the evolution of primordial reservoirs.

2 Methods

2.1 General physical properties

We model compressible thermochemical mantle convection using the finite volume code StagYY (Tackley, 2008). Each calculation is performed in a 2D spherical annulus domain, which emulates convection in a variable-thickness slice of a spherical shell centred at the equator (Hernlund & Tackley, 2008). The reference state characterizing compressible convection is based on the calculations presented in Tackley (1998). The parameters defining this reference state are listed in the Table S1 and illustrated in Figure S1 of the Supplement.

Thermochemical reservoirs are modelled with a dense primordial material origin. An initial dense layer occupies the bottom 160 km of the lower mantle, corresponding to a volume fraction of approximately 3%. The buoyancy ratio, B, defines the density contrast between regular and primordial materials, and depends on the radial profile of reference density (Text S1 and Equation S4 in Supplement). We fix its value to 0.23 in all simulations, which corresponds to a density contrast of 95 kgm^{-3} near the surface and 152 kgm^{-3} near the CMB. The mantle is basally heated and is also internally heated by heat-producing elements (HPEs) and we prescribe a non-dimensional heating rate, $H = 20$, which corresponds to a dimensional heating rate of 5.44×10^{-12} Wkg^{-1}. We assume a primordial material is enriched in HPEs and has a heating rate up to an order of mag-

nitude greater than regular mantle material. The initial temperature field is based on an adiabatic temperature profile of 2000 K with surface and core-mantle boundary layer thicknesses of approximately 30 km. Random temperature perturbations with an amplitude of 125 K are uniformly distributed throughout the domain. The surface and core-mantle boundary temperatures are defined at 300 K and 3440 K, respectively. Mantle viscosity featuring depth-, temperature-, and composition- dependence is modelled using an Arrhenius formulation. A factor of 30 viscosity contrast is imposed between lower mantle material and thermochemical reservoirs because dense material enriched in iron oxide and in bridgmanite (Trampert et al., 2004; Mosca et al., 2012) may be more viscous than regular (pyrolitic) mantle aggregate (Yamazaki & Karato, 2001). A yield stress of 290 MPa is imposed at the surface to avoid the development of a stagnant-lid. Viscosity is truncated so that nondimensional viscosity varies between 10^{-3} and 10^{5}.

We model a phase change between upper and lower mantle materials but neglect the phase change from perovskite (Pv) to post-perovskite (pPv) at the bottom of the mantle. Li et al. (2015) show that weak pPv (i.e., low viscosity contrast between Pv and pPv) and a low T_{CMB} (i.e., $T_{CMB} \sim 3350$ K) can result in the entrainment of primordial reservoirs. Because of our model setup, including a Pv-pPv transition may result in the entrainment of a dense primordial reservoir and mask the effect of thermal conductivity, which is the main aim of this study.

2.2 Thermal conductivity

Heterogeneous conductivity is emulated using a non-dimensional parametrized model that characterizes its variations with non-dimensional depth ($\tilde{d} = d/D$, where the depth, d, has a length scale defined by the mantle thickness, D), non-dimensional temperature ($\tilde{T} = T/\Delta T_S$, where the temperature, T, is scaled by the super-adiabatic temperature difference, ΔT_S), and composition, C, as separate functions. Thermal conductivity is non-dimensionalized with its surface value k_S, which is here fixed to $3 \, \mathrm{Wm^{-1}K^{-1}}$. The total conductivity is a product of each individual functional dependence.

For depth-dependence, we performed simulations with two different depth-dependence laws. First, we consider a linear depth- dependence given by

$$\tilde{k}_D(\tilde{d}) = 1 + (K_D - 1)\tilde{d} \tag{1}$$

where K_D specifies the bottom-to-top conductivity ratio. The non-dimensional depth- dependent conductivity thus takes on values between 1 and K_D. Next, we consider depth- dependence based on conductivity measurements of minerals in the upper and lower mantles. Conductivity values in the lower mantle were based on a parametrization of conductivity profiles (defined in Deschamps & Hsieh (2019)) for a 80%-bridgmanite (Bm) and 20%-ferropericlase (Fp) mixture. Measurements for bridgmanite were presented by Hsieh et al. (2017) and for ferropericlase by Hsieh et al. (2018). The conductivity profile in the upper mantle is defined by a quadratic curve that smoothly connects the surface conductivity to the conductivity profile of Bm-Fp at the 660-km transition. We find that there is good agreement between the modelled conductivity profile and the measurements of dry and wet olivine presented by Chang et al. (2017). The total conductivity profile is defined piecewise and continuous at the

660-km transition ($\tilde{d}_{ULM} = 0.22837$, see Figure 1) and is given by

$$155 \quad \tilde{k}_D(\tilde{d}) = \begin{cases} \frac{3.0}{k_S}\left(1 + 15.66\tilde{d} - 16.38\tilde{d}^2\right); & \tilde{d} < \tilde{d}_{ULM} \quad \text{(Upper mantle)} \\ \frac{5.33}{k_S}\left(1 + 4.98\tilde{d} - 0.81\tilde{d}^2\right); & \tilde{d} \geq \tilde{d}_{ULM} \quad \text{(Lower mantle)} \end{cases} \tag{2}$$

The bottom-to-top conductivity ratio is 9.185 and this depth- dependence is referred to as K_{DH} in this study. Compared with the linear $K_D = 10$ depth- profile, the quadratic depth- dependence is slightly raised near the transition zone and slightly lowered near the CMB. Depth- dependent conductivity profiles are illustrated in Figure 1.
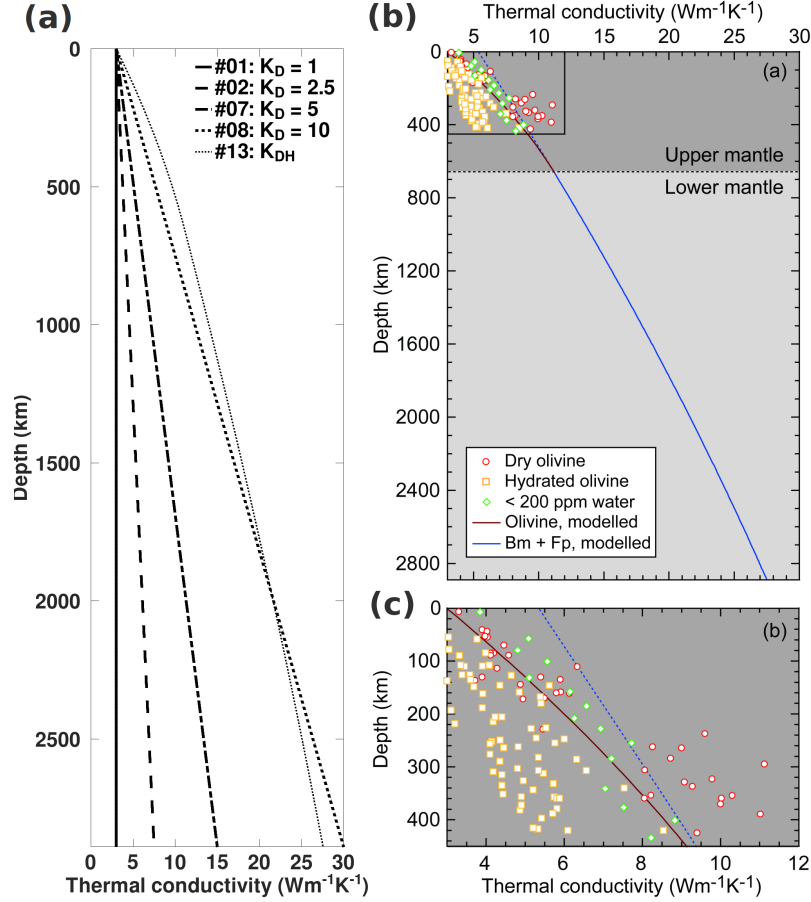
Figure 1. (a) Radial profiles for different depth- dependent conductivity functions characterized by different K_D values. (b) Conductivity measurements for upper and lower mantle materials. Olivine data points are from Chang et al. (2017) and the modelled Bm+Fp conductivity profile is based on data presented in Hsieh et al. (2017) and Hsieh et al. (2018). (c) Magnification of conductivity profile in the upper mantle.

The temperature- dependence is given by

$$160 \quad \tilde{k}_T(\tilde{T}) = \left(\frac{(T_{surf}/\Delta T_S)}{\tilde{T}}\right)^n, \tag{3}$$

which always decreases thermal conductivity relative to the values defined in the depth- dependent profile when $T > T_{surf}$. The super-adiabatic temperature difference, ΔT_S, is set to 2500 K. Higher values of n indicate higher sensitivity to (and thus greater reduction with) increasing temperature. In this study, we consider n values of 0.5 and 0.8. The theoretical lower limit for n is 0.5, for materials that are enriched in iron, and a value of 0.8 is representative of oxides (e.g., Klemens, 1960; Xu et al., 2004). When n is 0.0, temperature- dependence is switched off and only the remaining dependences are considered.

The composition- dependence is given by

$$\tilde{k}_C(C) = 1 + (K_C - 1)C \tag{4}$$

where K_C is the reduction factor for composition- dependence. For the primordial material considered in this study we consider 20% and 50% conductivity reduction (corresponding to $K_C = 0.8$ and 0.5, respectively), which encompasses a 26% reduction in conductivity for LLSVPs estimated by Deschamps & Hsieh (2019). When K_C is 1.0, composition dependence is switched off. Finally, the total conductivity is given by

$$k(d, T, C) = k_S \times \tilde{k}_D(d) \times \tilde{k}_T(T) \times \tilde{k}_C(C). \tag{5}$$

Figure 2 shows the initial temperature (left panel) and conductivity profiles (right panel) that correspond to models featuring a depth- dependence (K_{DH}) based on conductivity measurements of upper and lower mantle minerals. Different combinations of temperature- and composition- dependence are presented to show the degree of conductivity reduction resulting from these dependencies. The purely depth- dependent model ($n = 0$) has a conductivity of 27.6 $\mathrm{Wm^{-1}K^{-1}}$ at the CMB. For the T_{CMB} we consider (e.g., 3440 K), the conductivity at the CMB will be reduced by approximately 70% and 86% for $n = 0.5$ and 0.8 leading to conductivities of 8.1 and 3.9 $\mathrm{Wm^{-1}K^{-1}}$, respectively. For primordial material at that depth, a 20% reduction suggests conductivities of 22.0, 6.5, and 3.1 $\mathrm{Wm^{-1}K^{-1}}$ for $n = 0, 0.5$ and 0.8, respectively. Note that because the piles are enriched in HPEs, their conductivities will decrease as they heat up.

Because conductivity is allowed to vary throughout the system, the governing equation for conservation of energy given by

$$\bar{\rho}C_P \frac{DT}{Dt} = -\mathrm{Di}_{surf} \bar{\alpha} \bar{\rho} T v_Z + \nabla \cdot (k \nabla T) + \bar{\rho} H + \frac{\mathrm{Di}_{surf}}{Ra} \Phi. \tag{6}$$

The physical parameters in this equation include the reference density, $\bar{\rho}$; the reference heat capacity, $\bar{C}_P$; the reference thermal expansivity, $\bar{\alpha}$; the vertical velocity, v_Z; the surface dissipation number, Di_{surf}; the heat production, H; the reference Rayleigh number, Ra; and the viscous dissipation, Φ. The thermal conductivity, k, is included in the heat diffusion term $\nabla \cdot (k \nabla T)$. One important consequence of heterogeneous conductivity is that the diffusion of heat through hot (piles or plumes) and cold (downwellings) regions is reduced and enhanced, respectively.

2.3 Model setup

Simulations are computed over a non-dimensional diffusion time of 0.0318, corresponding to 11.2 Gyr in dimensional units. Each simulation starts with a transient phase during which the basal layer of dense material heats up, and whose duration depends on the input parameters. Note that because they do not include mantle initial conditions, which are not known, and
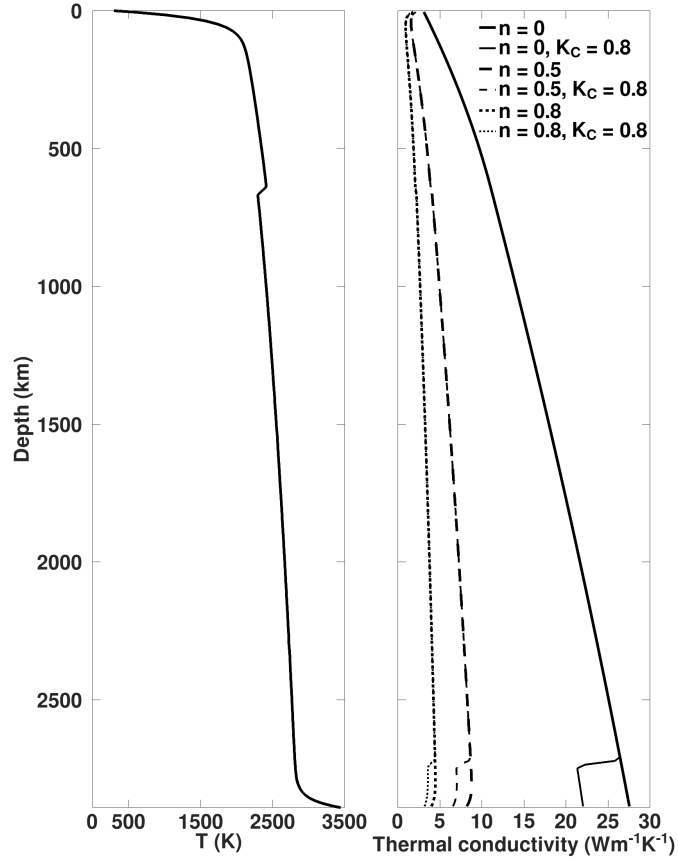
Figure 2. Initial temperature profile (left panel) for all cases and sample initial conductivity profiles (right panel) for cases featuring K_{DH}.

time-decreasing radioactive heating, our simulations are not meant to model the mantle evolution, and therefore durations should not be used to interpret specific sequences of events. The longer simulation time is necessary to allow the simulations to achieve a quasi-steady state, during which the surface and CMB heat flows oscillate around nearly constant values. In addition, it is possible that shorter simulation times (i.e., 4.5 Gyr) may lead to a premature conclusion that primordial reservoirs have reached a metastable state. For systems with heterogeneous conductivity and constant heating conditions, significant changes in the evolution of thermochemical reservoirs may take longer to manifest. Using this setup, we run 24 simulations exploring the impact of conductivity variations (Table 1) with values of n, K_D, and K_C in the range 0-0.8, 1-10, and 0.5-1.0, respectively. All observable and derived physical properties are averaged over a 2 Gyr window centred about $t = 4.5$ Gyr (illustrated in Figure 7) and are presented in Table 1. As the system evolves after 4.5 Gyr, the pile volume diminishes and the core-mantle boundary surface is further exposed. The surface and core-mantle boundary heat flows oscillate about different values in a new quasi-steady state. However, pile statistics including mean temperature and average height differ compared to its previous quasi-steady state. The averaged properties centred about 9.0 Gyr and averaged from 3 to 11.2 Gyr are presented in the

Supplement (Table S2 and Table S3, respectively). In general, while the A_{CMB} values have decreased, the trends referred to
in the figures still hold. Complete details of the methods are included in the Supplement.

3   Results

To measure the evolution of the thermochemical structure, we examined our calculations once they became quasi-stationary, as
defined by the mean core-mantle boundary heat flow, Q_{CMB}, and surface heat flow, Q_{SURF}. The stability of thermochemical
reservoirs was assessed by their mean temperature, T_{prim}; average height, h_C (defined in the Supplement); and coverage of
the CMB, A_{CMB}. The onset of instability, $t_{inst.}$, is calculated by examining time derivatives of average heights of primordial
material (see the Supplement for details). We now examine the individual influences of conductivity changes with depth,
temperature, and composition.

3.1   Effect of purely depth- dependent conductivity

First, we isolated the effect of purely depth- dependent conductivity. Relative temperature, primordial material, and conduc-
tivity fields are presented in Figure 3. In Figure 3 and all subsequent figures, the temperature fields are offset relative to the
core-mantle boundary temperature ($T_{rel,CMB} = T - T_{CMB}$) to help illustrate temperature excesses (or deficits) within the
piles. When we increase K_D from 1 to 10, we observe a decrease in the mean temperature of the piles (T_{prim}) (from 3930
K down to 3410 K) and an increase in the mean mantle temperature (T_{mean}) (from 2150 K up to 2290 K) because the piles
transfer their heat to the ambient mantle more efficiently.

From the primordial material fields, we observe that a modest conductivity gradient ($K_D = 2.5$) is sufficient to stabilize the
thermochemical reservoirs and stimulate a 2-pile configuration (by 4.5 Gyrs) (compare plots (e) to (h)). This finding lends
credence to pile configurations obtained by models that had adopted the canonical increase of conductivity by a factor of 2.5
from surface to core-mantle boundary. As K_D is further increased, reservoirs progress toward an antipodal arrangement. In
addition, the mantle flow becomes less turbulent since the increased thermal conductivity (and by extension thermal diffusivity)
decreases the effective Rayleigh number.

Comparing between each K_D case, for some arbitrary thermal gradient between piles and ambient mantle, a greater lower-
most mantle conductivity will result in more efficient heat extraction; and thus a lower mean pile temperature. Furthermore,
the heat flow at the core-mantle boundary is also increased (from 4.6 TW up to 14.7 TW, for K_D between 2.5 and 10), which
encompass the lower and upper limits predicted for the Earth (Jaupart et al., 2007). Note that the greatest bottom-to-top conduc-
tivity ratio we consider, $K_D = 10$, implies a conductivity value of 30 $\mathrm{Wm^{-1}K^{-1}}$ at the CMB. However, the predicted thermal
conductivities in the lowermost mantle do not exceed 10 $\mathrm{Wm^{-1}K^{-1}}$. Therefore, temperature- dependence, which reduces the
thermal conductivity, must be considered.
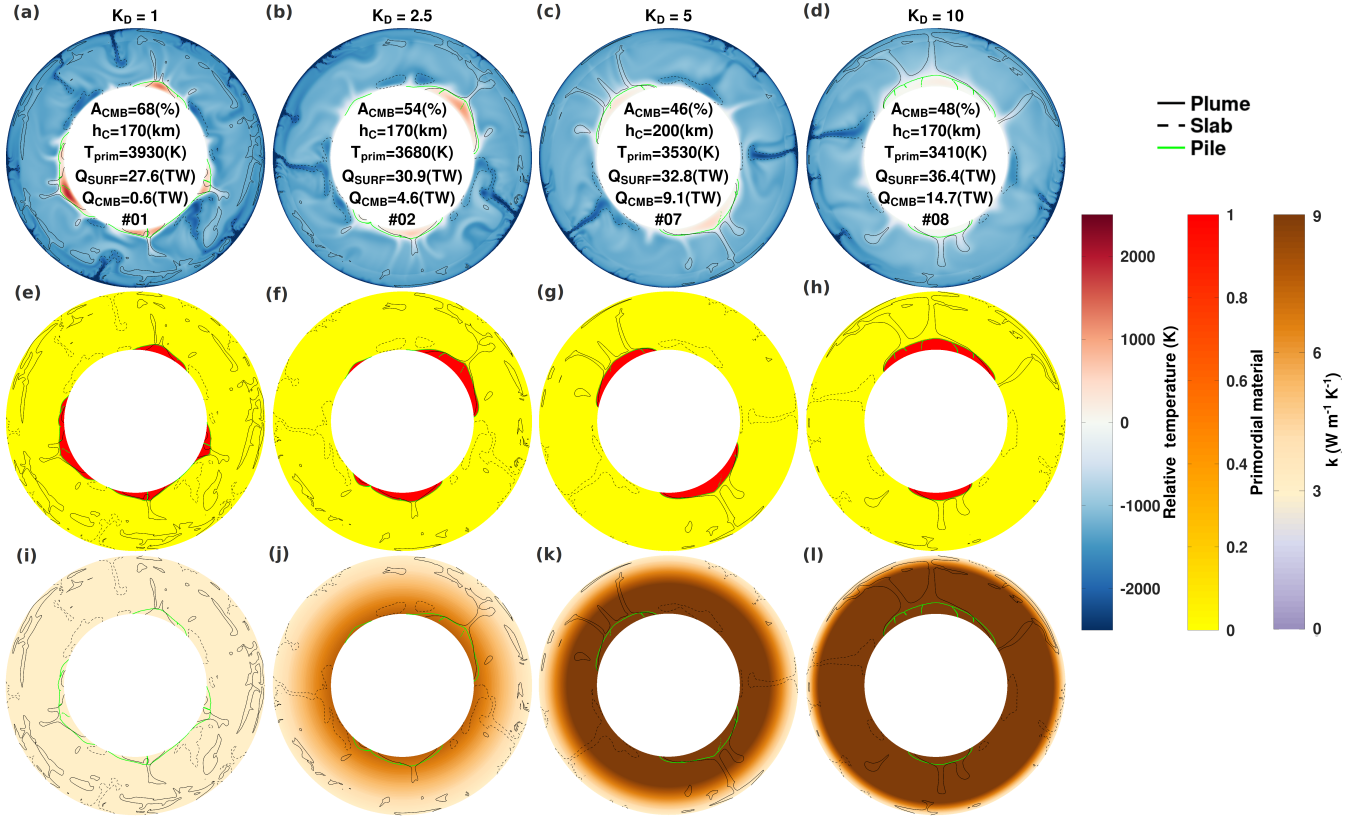
Figure 3. Temperature (relative to the CMB temperature) (top row), primordial material (centre row), and conductivity (bottom row) fields at 4.5 Gyr are shown as a function of K_D. Contours are indicated in the legend and field values are indicated on the colour bars. The conductivity colour bar saturates at $9 \mathrm{~Wm}^{-1}\mathrm{K}^{-1}$ so that the values in (k) and (l) may be larger. Averaged properties and case numbers are inset.

Table 1. Averaged properties for all cases presented. Supplemental cases are indicated by a letter 'S'. All values are computed within in a 2 Gyr period encompassing 4.5 Gyr.

Case #	K_D	K_C	n	T_{mean} (K)	T_{prim} (K)	global rms dT_{prim} (K)	negative rms dT_{prim} (K)	positive rms dT_{prim} (K)	$\Delta T_{prim,max}$ (K)	Q_{SURF} (TW)	Q_{CMB} (TW)	h_C (km)	A_{CMB}(%)	$t_{inst.}$ (Gyr)
1	1	1	0	2150	3930	450	350	550	1400	27.6	0.6	170	68	5.8
2	2.5	1	0	2200	3680	280	220	330	770	30.9	4.6	170	54	9.2
3	2.5	1	0.5	2370	4150	610	510	720	1480	23.3	-0.6	200	74	5.2
4	2.5	0.8	0.5	2380	4330	670	600	740	1530	24.1	1.1	290	55	4.9
5	2.5	0.5	0.5	2390	4420	740	660	830	1830	23.3	0.5	400	64	4.5
6	2.5	1	0.8	2500	4700	770	750	790	1620	22.2	0.2	380	51	4.5
7	5	1	0	2230	3530	150	130	170	400	32.8	9.1	200	46	>11.2
8	10	1	0	2290	3410	90	110	80	190	36.4	14.7	170	48	>11.2
9	10	1	0.5	2400	3710	260	210	320	730	26.8	3.5	170	58	>11.2
10	10	0.8	0.5	2410	3850	360	300	440	870	26.3	4.6	200	46	8.4
11	10	0.5	0.5	2390	3760	320	270	370	890	24.8	3.5	170	58	9.0
12	10	1	0.8	2490	3950	470	380	570	1200	21.6	0.3	140	68	8.2
13	DH	1	0	2260	3400	90	120	70	710	37.6	13.5	170	53	>11.2
14	DH	0.8	0	2250	3450	110	120	110	270	38.5	15.5	200	41	>11.2
15	DH	1	0.5	2370	3620	200	170	230	560	26.6	3.3	140	60	>11.2
16	DH	0.8	0.5	2380	3700	270	220	330	780	26.5	3.6	170	59	11.1
17	DH	0.5	0.5	2380	3820	420	320	520	1110	25.6	3.0	170	64	8.8
18	DH	0.8	0.8	2470	4190	530	480	580	1170	22.7	1.5	200	49	6.6
S1	1	1	0.5	2380	4640	770	780	770	1540	23.7	1.0	750	36	3.9
S2	1	1	0.8	2510	4900	820	830	810	1780	21.8	0.6	930	36	4.1
S3	5	1	0.5	2400	4050	490	400	580	1230	25.2	2.3	200	47	6.0
S4	5	1	0.8	2490	4380	680	640	710	1430	21.4	0.0	200	61	5.4
S5	5	0.8	0.5	2400	4160	560	480	640	1330	24.5	2.4	200	47	5.6
S6	5	0.5	0.5	2410	4210	620	530	730	1530	23.9	1.7	230	57	5.2

3.2 Effect of temperature- and depth- dependent conductivity

Next, we examine the combined effects of depth- and temperature- dependence. Figure 4 shows the relative temperature and thermal conductivity fields for end-member cases featuring $K_D = 2.5$ and 10 (similar plot for $K_D = 5$ is shown in Supplement Figure S5), and Supplement Figures S3 and S4 plot the corresponding radial profiles. The effect of temperature clearly appears on the conductivity fields. Compared to the purely depth- dependent cases, thermal conductivity is strongly reduced throughout the mantle, and the depth dependence is strongly attenuated. By contrast, lateral variations in conductivity can be observed between hot (less conductive) piles and cold (more conductive) downwellings.

For $K_D = 2.5$, the lowest non-zero n value tested (i.e., 0.5) results in a 70% reduction in conductivity (from 7.5 $\mathrm{Wm^{-1}K^{-1}}$ down to approximately 2.2 $\mathrm{Wm^{-1}K^{-1}}$ (see conductivity profiles in Figure S3)) at the core-mantle boundary and a mean bottom-to-top conductivity ratio is < 1. This reduction is further amplified with greater n values. The piles evolving under these conductivity conditions move towards a more asymmetric configuration and may take on a columnar morphology (Figure 4(c)). Overall, temperature- dependence of conductivity results in a lower conductivity at the bottom of the mantle, with mean bottom-to-top conductivity ratio < 1, which promotes thermochemical piles instability, as poorly conducting piles retain more heat and become more thermally buoyant.

For $K_D = 10$, the thermal effect on conductivity as n was increased is compensated by the strong increase of conductivity with depth, and a mean bottom-to-top conductivity ratio larger than 1 is established (e.g., Figure 4 plots (k) and (l), resulting in a 2-pile arrangement). For instance, a mean conductivity ratio ≥ 2 is produced for $K_D = 10$ and $n = 0.5$. The horizontally averaged conductivities near the CMB are brought closer to predicted values for the Earth's lower mantle (~ 8 $\mathrm{Wm^{-1}K^{-1}}$ (case #9)) and are much lower compared to the purely depth-dependent cases (30 $\mathrm{Wm^{-1}K^{-1}}$ (case #8), for $K_D = 10$; Figure S4).

For cases featuring $K_D = 5$ (see Figure S5), increasing pile temperature with temperature dependence is also observed. Because the resulting mean bottom-to-top conductivity ratio is > 1, pile morphology tends to be more dome-like and evolution is similar to cases with $K_D = 10$. Trade-offs between the temperature- and depth- effects on the lowermost mantle conductivity (and the mean bottom-to-top conductivity ratio) can be observed. For instance, case #12 in Figure 4(l) and case #S3 in Figure S5(h) (and case #3 in Figure 4(h) and case #S4 in Figure S5(i)) demonstrate that equivalent conductivity fields may be obtained by systems characterized by greater combined depth- and temperature- dependence or lesser combined depth- and temperature-dependences

The pile configuration and downwelling planform influence one another and evolve in parallel. Specifically, within the first 2 Gyr, the initial downwelling currents determine the initial subdivision of the primordial reservoir that further determine the upwelling currents. As the system evolves further, the impact of returning downwelling flow depends on the relative density of the primordial material. The latter depends on the thermal evolution and hence on the conductivity of the piles. When conductivity of piles is greater (i.e., mean bottom-to-top conductivity ratio > 1), the piles remain cooler and more dense compared to downwelling currents. Thus, the bulk accumulation of primordial material remains approximately fixed in place and the thinner margins get pushed laterally by downwelling currents. We find that long-lived degree-2 thermochemical structure and down-
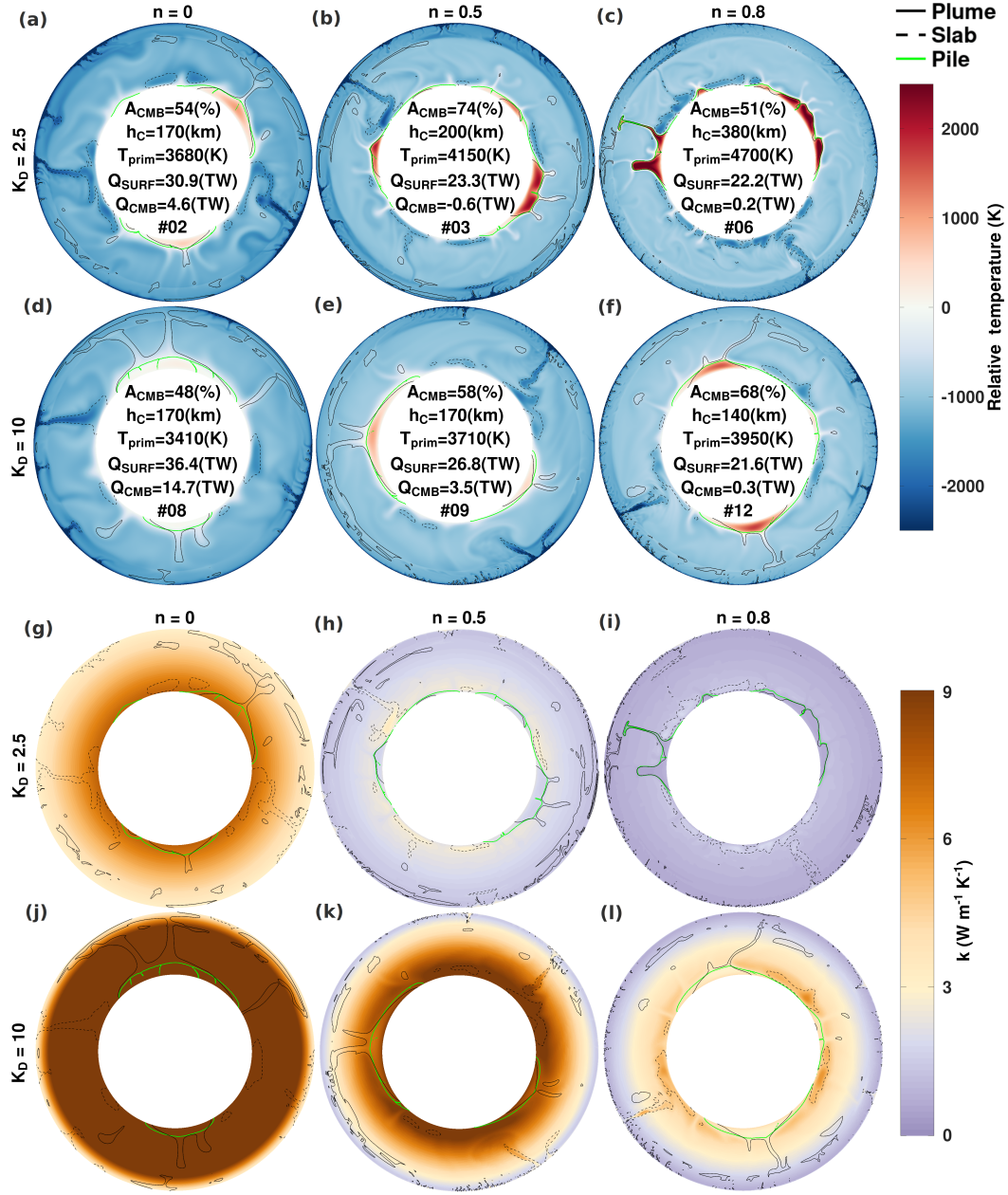
Figure 4. Temperature fields (relative to the CMB temperature) and conductivity fields at 4.5 Gyr are shown for cases as a function of K_D and n. Contours are indicated in the legend and field values are indicated on the colour bars. The conductivity colour bar saturates at 9 $\text{Wm}^{-1}\text{K}^{-1}$ so that the values in (j) and (k) may be larger. Averaged properties and case number are inset. (Primordial material fields are illustrated in Figure S2.)

welling planforms are found for bottom-to-top conductivity ratios > 2. Given the trade-offs between depth- and temperature-dependences, a set of K_D and n that produce a bottom-to-top conductivity ratio of 2 can be computed using Equation 5 for any particular T_{CMB}.

We observed that T_{prim} increased with greater temperature dependence (columns viewed left-to-right in Figure 4). Because piles' conductivity is reduced with increasing n, piles become less prone to losing their heat to the mantle and piles' temperature increases. However, temperature still decreased with an increased depth-dependent gradient, K_D (e.g., cases #4 and #10 and cases #5 and #11 in Figure 4), but to a lower extent than in the purely depth- dependent cases. For cases with a mean conductivity ratio < 1, pile temperature increases significantly so that a T_{prim} in excess of 500 K of the T_{CMB} (e.g., cases #1, #3 and #6 and cases #S1, #S2, and #S4) is obtained. Because the temperature excess causes a negative temperature gradient between the piles and the CMB, a locally negative bottom heat flux within piles is obtained. The evolution of the piles in these cases tends to eventual entrainment. In those systems, entrainment is typically preceded by columnar pile morphologies that become too thermally buoyant and eject blobs of primordial material. When piles retain more heat, temporal variations in the mean height of the piles due to thermal buoyancy are more rapid than the deformation by downwelling currents. The timing for the onset of instability, $t_{inst.}$, is listed for each case in Table 1. Pile's stability depends on how efficiently it can rid itself of heat. We find that greater heat extraction can be achieved for conductivity models characterized by $K_D = 10$ and that temperature dependence can emulate conductivities relevant to Earth's lowermost mantle. Because composition (i.e., iron enrichment) also attenuates piles' conductivity, this effect must be examined in conjunction with temperature and depth's influence on the mantle's mean conductivity ratio.

3.3 Including the effect of composition- dependent conductivity

The effect of composition- dependence is highlighted in Figure 5 for the cases featuring $K_D = 2.5$ and 10 with $n = 0.5$. For the cases featuring $K_D = 2.5$, composition- dependence further reduces the conductivity of piles below the conductivity of the ambient mantle at lowermost mantle depths (Figure 5 panels (h) and (i)). Although small, the reduction of pile conductivity due to composition- dependence amplifies the behaviour observed for temperature- dependent cases with similar depth- dependence (i.e., a decrease in the piles' stability) and results in earlier instability (see Figure S11).

Similarly, for the $K_D = 10$ case, accounting for composition- dependence of conductivity amplifies the effects induced by temperature- dependence. In addition, the magnitude of the reduction in conductivity is also amplified. The percentage conductivity difference at a depth of 2500 km (i.e., at a depth adjacent to the bulk of the piles) is $\sim 40\%$ when $K_C = 0.8$, and $\sim 60\%$ when $K_C = 0.5$. This conductivity difference between piles and the ambient mantle induces a minor increase in pile temperature that grows over time. When $K_C = 0.8$, this increase in temperature leads to a slowly manifesting thermal instability that results in a bulk ejection of primordial material by 8.4 Gyr. However, the entrainment of the piles does not occur shortly after this episode of ejection (see Figure S12).

For the intermediate depth- dependent case $K_D = 5$ (Figure S9), the mean lowermost mantle conductivity is greater than the surface conductivity and does not vary significantly when the conductivity of primordial material is reduced (i.e., < 1 $Wm^{-1}K^{-1}$ in the lowermost mantle; Figure S10). The maximum conductivity, characterized by the remnant downwelling
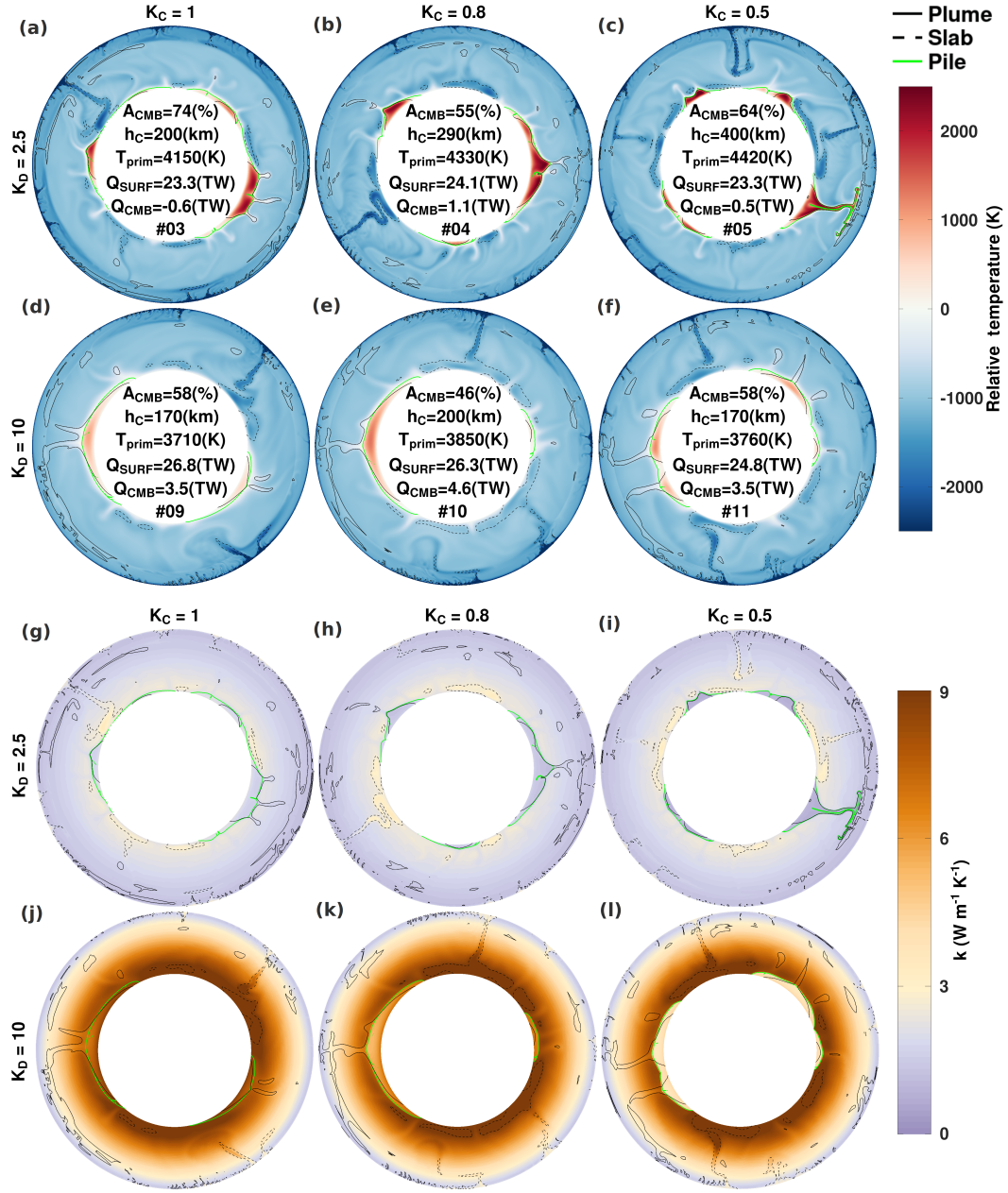
Figure 5. Temperature (relative to the CMB temperature) and conductivity fields at 4.5 Gyr are shown as a function of K_D and K_C when $n = 0.5$. K_C is increases from right to left. Contours and inset values are defined similarly as in Figure 4. The conductivity colour bar saturates at $9 \, \mathrm{W m^{-1} K^{-1}}$ so that the values in (j), (k), and (l) may be larger. (Primordial material fields are illustrated in Figure S6.)

material localized within the bottom 300 km, is approximately 2 $\mathrm{Wm^{-1}K^{-1}}$ higher than the mean conductivity profile. The minimum conductivity, characterized by the hottest regions of the reservoirs, is approximately 2 $\mathrm{Wm^{-1}K^{-1}}$ lower than the mean, and is localized near the tops of the piles, where the hottest and most buoyant primordial material accumulates (approximately 500 – 800 km above the CMB). Pile temperature marginally increased when K_C was reduced. The additional thermal buoyancy imparted into the piles quickened the onset of instability. For this K_D value, the erosion of piles is initiated approximately 0.4 Gyr and 0.8 Gyr earlier from 6 Gyr when $K_C = 0.8$ and $K_C = 0.5$, respectively. Furthermore, pile configuration may change. When $K_C < 1$, single pile configuration can be attained as early as 8 Gyr (Figure S13). At all depth- dependences tested, we found that the effect of composition- dependence was small compared the dominant temperature- dependent effect. Nevertheless, at greater depth- dependences, the compounded conductivity reduction is amplified, and thermal instability within piles is inevitable. Comparing cases when composition- dependence is neglected or is considered, the difference in $t_{inst.}$ is greater when depth- dependence is greater.

3.4 Long-term stability of thermochemical reservoirs featuring mineral physics derived conductivities
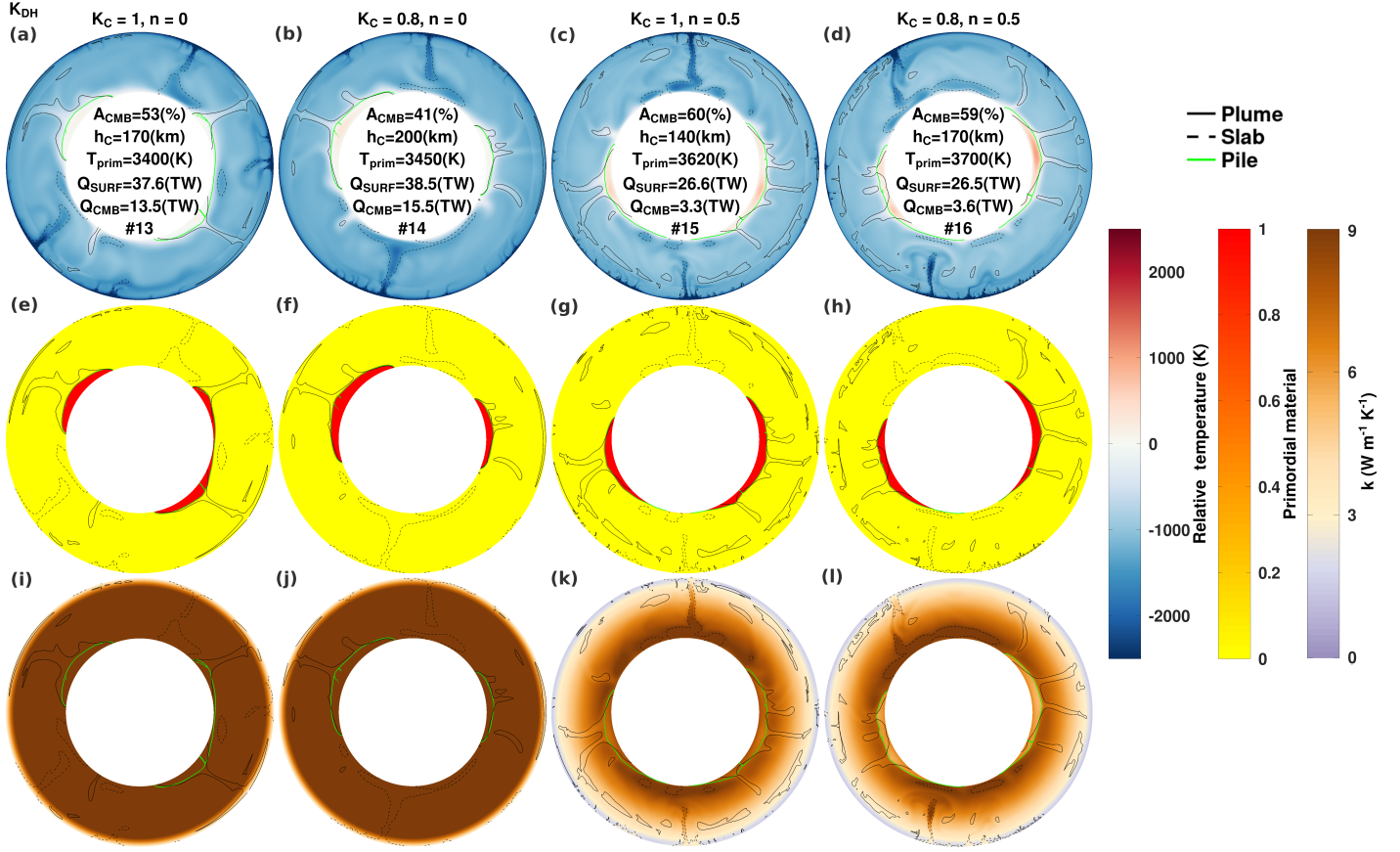
Figure 6. Temperature (relative to the CMB temperature) (top row), primordial material (middle row), and conductivity (bottom row) fields at 4.5 Gyr are shown for cases featuring K_{DH}. Contours and inset values are defined similarly as in Figure 4. The conductivity colour bar saturates at 9 $\mathrm{Wm^{-1}K^{-1}}$ so that the values in (i) - (l) may be larger. Inset values are defined similarly as in Figure 4.

Finally, we examine the effect of depth- dependence, based on measured conductivities of upper and lower mantle minerals (Hsieh et al., 2017, 2018), on the long-term stability of thermochemical reservoirs. First, we isolate the effects of temperature 315 ($n = 0.5$) and composition ($K_C = 0.8$) in conjunction with mineral conductivities. Second, we construct the fully heterogeneous thermal conductivity model ($n = 0.5$ and $K_C = 0.8$; case #16), which we use as a reference case. We find that the resulting lower mantle conductivities for this reference case are comparable to current estimates (e.g., Geballe et al., 2020). Figure 6 indicates that for given values of n and K_C, models obtained with the mineral physics depth- dependence are very similar to those obtained with linear depth dependence with $K_D = 10$ (see Figure 4 and 5 for comparison). Heat flows for our models 320 reached a quasi-steady state by approximately 4 Gyr (Figure 7). We found that temperature- dependent conductivity greatly reduced both CMB and surface heat flows (by approximately 73% and 30%, respectively), as less heat can be extracted from
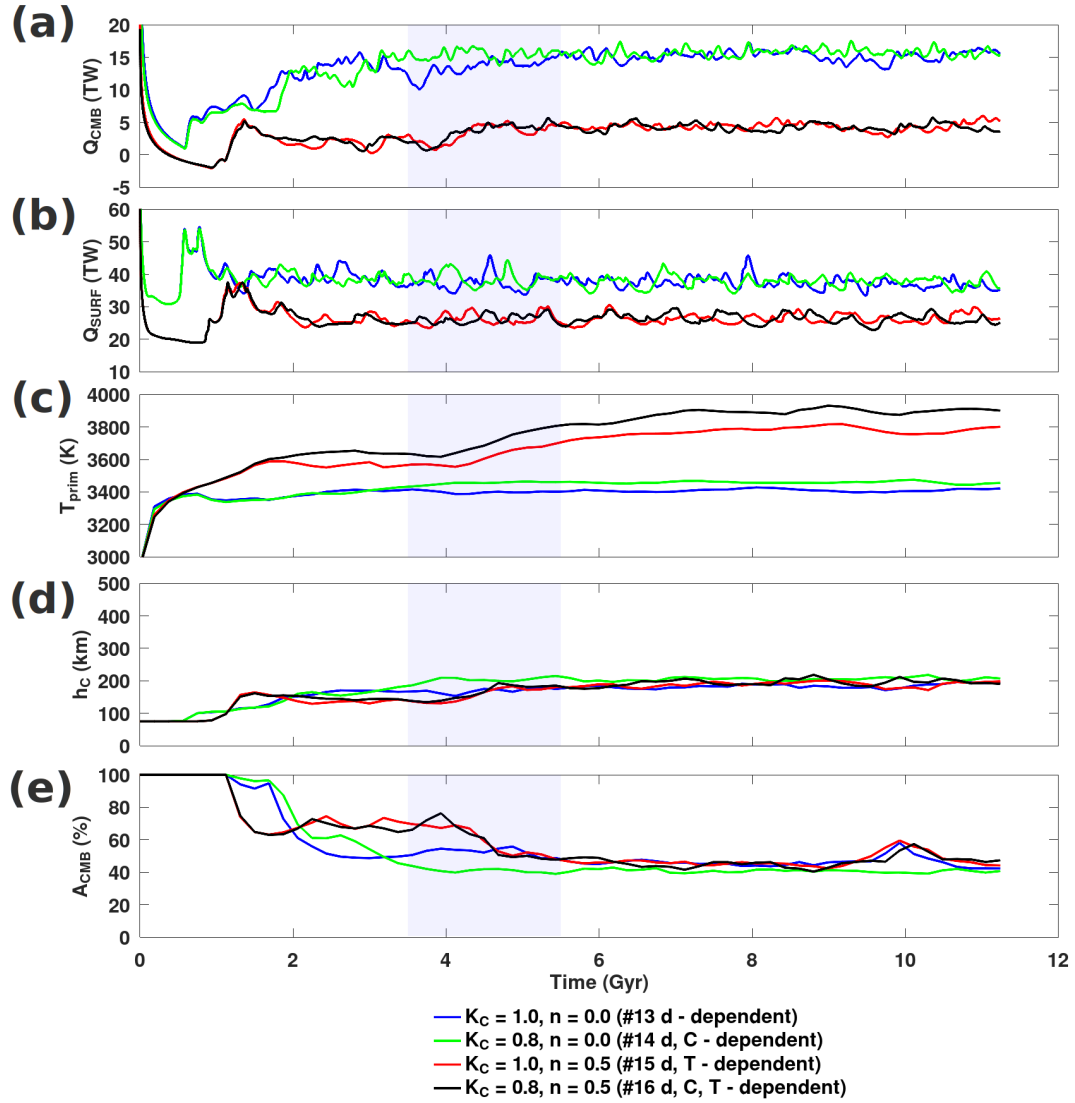
Figure 7. Evolution of cases featuring K_{DH} corresponding to those presented in Figure 6. The quasi-stationary period centred about 4.5 Gyr is shaded in gray.

the base. Furthermore, we find that composition- dependence is of secondary importance, in agreement with Li et al. (2022)'s findings. Despite a 20% reduction in the conductivity of primordial material (green), Q_{CMB} is marginally greater (by 2 TW). Similarly, Q_{CMB} is marginally greater when temperature- dependent conductivity included composition- dependence (by 0.3 TW). This behaviour is likely owing to less CMB coverage in composition- dependent cases. Differing conductivity conditions can result in many thermochemical reservoir evolution and cooling histories. For the cases examined in Figure 6, we found that the mean height of piles and CMB coverage approached a quasi-steady value. However, T_{prim} greatly increased when

325

temperature dependence was considered. For systems with a temperature- dependent conductivity (i.e., red or black curves), piles slowly heat up during their long-standing CMB coverage. Piles' gained thermal buoyancy increased their height (thus,

330   exposing the core-mantle boundary surface to the cooler ambient mantle) and allowed more heat to be extracted from the core. Determining the mechanisms that trigger different outcomes will provide constraints for plausible mantle conductivity models.
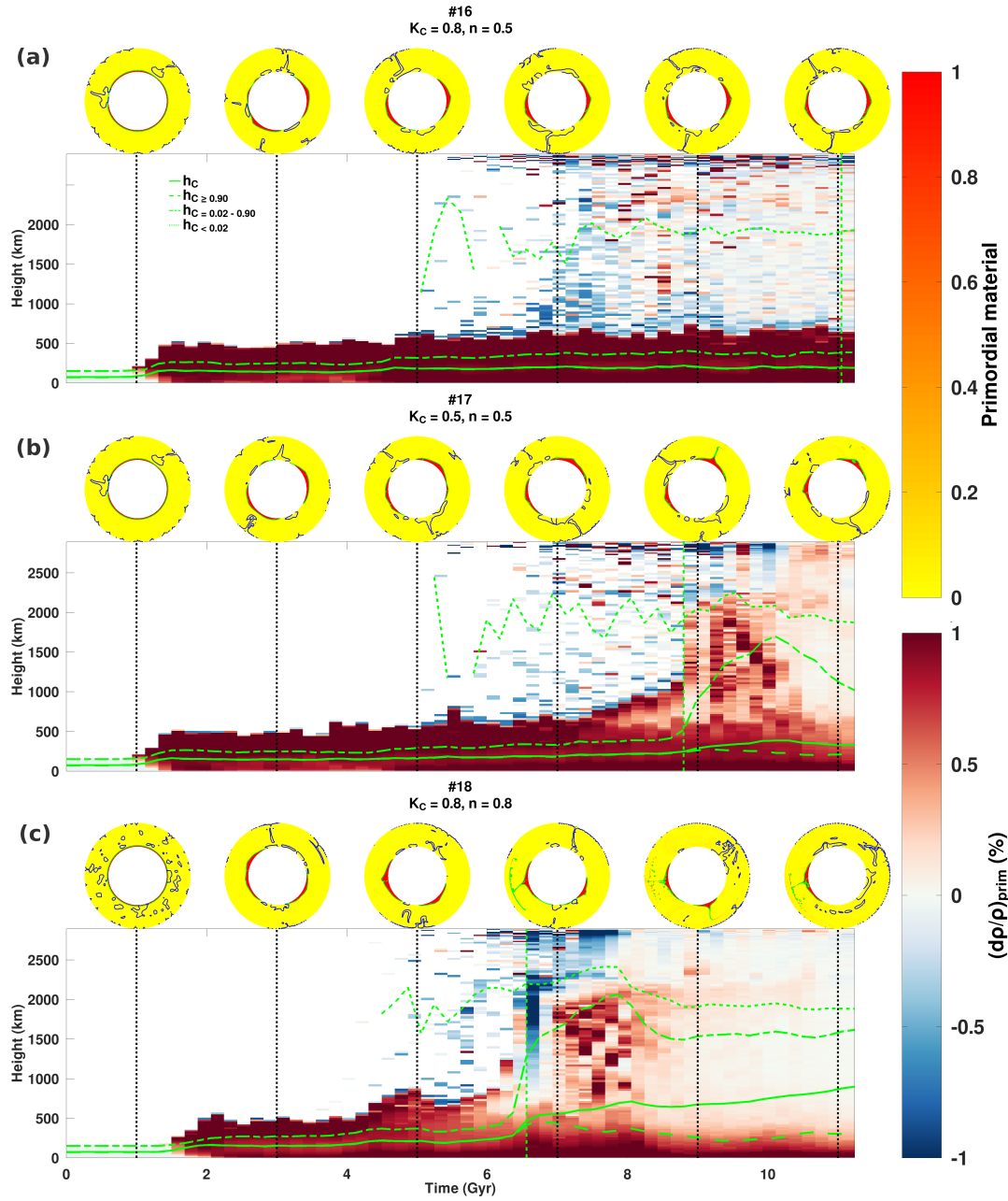
Figure 8. Evolution of the horizontally averaged primordial material density anomalies is illustrated for cases featuring K_{DH}. Primordial field snapshots are sampled at 2 Gyr intervals starting at 1 Gyr above the timeseries (dashed-black vertical line indicates the time). Mean heights of primordial material are plotted on top of the density anomaly timeseries. The dashed-green vertical line indicates the onset of instability in thermochemical reservoirs. In the snapshots, downwelling structures are indicated by solid blue contours and piles are indicated by solid green contours.

Figure 8, plotting the heights of primordial material (for different ranges of C) in conjunction with the horizontally averaged density anomalies as a function of time, illustrates the evolution of the thermochemical structure for cases with different n and K_C. Because the horizontally averaged profiles mask the spatial distribution, primordial field snapshots with 2 Gyr intervals are also indicated for reference. The average heights and vertical variations in the density anomaly profiles evolve synchronously, correspond to the same measure of instability, $t_{inst.}$, and can capture changes in individual pile behaviour (with confirmation in the primordial field snapshots). Figure 8 may be used to examine departures from the reference moderate temperature- dependence ($n = 0.5$) and composition- dependence ($K_C = 0.8$) (case #16). The variations in average height do not discriminate between 'intrinsic' (i.e., thermal buoyancy) or 'extrinsic' (i.e., downwellings) deformation. However, the influence of downwellings can be observed following the transient period (on the density anomaly timeseries, the initial transient period is characterized by the flat average height curves overlying the white layer below 200 km). For cases #16 and #17, the transient period lasts approximately 1 Gyr and for case #18 approximately 1.5 Gyr. The first downwellings impinge on the initial dense layer but do not result in a rapid uplift of material (sufficient to eject blobs of dense material). Once the initial dense layer has organized into piles, downwellings tend to move dense material laterally over the CMB but do not increase rapidly the pile height. Nevertheless, we find that it is easier for downwelling currents to push primordial material that has been made lighter due to their retained heat.

Different initial conditions altering the thermal histories of case #17 are examined to check the robustness of our findings. We consider lower and higher initial mantle temperatures, T_{init}, of 1750 K and 2250 K and temperature perturbations, dT, of 375 K are added to cases with $T_{init} = 2000$ K and 2250 K (see Figure S15 for the radial profiles and Table S4 for model averages in the Supplement). Overall, initial conditions on temperature control the duration of the initial transient phase, but do not substantially alter the subsequent evolution of the system. In particular, greater dT does not significantly alter the influence of initial downwellings or the evolution of piles and $t_{inst.}$ is approximately 0.2 Gyr later (Figure S16(a),(b)). In addition, $t_{inst.}$ is approximately 2 Gyr earlier (1 Gyr later) for systems with hotter (cooler) T_{init} (Figure S17). A greater dT further decreases $t_{inst.}$ when $T_{init} = 2250$ K (Figure S16(c)). The different histories (with similar downwelling planforms) show that the onset of instability within piles is an intrinsic thermal effect and hotter thermal conditions are also consistent with this finding.

In the reference case, thermochemical convection exhibits a stable 2-pile configuration during the entire simulation. The total pile height can be roughly read from the density anomaly plot (i.e., the initial sharp contrast in colour between red and white). For stable piles, the average heights of the pile (h_C) will then be roughly less than half of their maximum pile height. (Average height is calculated based on volumetric weighting in a spherical geometry (see Supplement Section 3.3).) These primordial reservoirs remain highly concentrated with a thin veneer of less concentrated material (from mixing with the ambient mantle) covering the piles. Thus, the average height of the veneer ($h_{C=0.02-0.90}$) is slightly greater than the average height of the piles because it is localized at the top and sides of the reservoirs. In Figure 8, $h_{C=0.02-0.90}$ is indicated in the timeseries by dot-dashed green curves and on the primordial field snapshots by the solid green contours. The average heights are weighted with respect to the primordial material field C, when buoyant primordial structures (i.e., columnar plumes or ejected blobs) are present, their average heights cannot be distinguished compared to the lower-lying piles if only material with $C > 0.90$ is considered. Because the volume of material in the veneer is much lower compared to piles, its average height can be differentiated

from the piles and the onset of thermal instability is easier to analyse using this metric. For the reference case, the slow erosion of the least concentrated primordial material ($C < 0.02$) from this veneer occurs after 5 Gyr. From the temporal variations in average heights, we find that thermal instability appears to manifest very late in the simulation run time (after approximately 11 Gyr), which is consistent with the gradual accumulation of heat within the piles (observed in the slowly increasing mean pile temperature (see Figure 9(c))).

When only K_C is reduced, from 0.8 to 0.5 (case #17), a 2-pile configuration is also maintained throughout the simulation, but episodes of bulk erosion in thin plume conduits are possible (e.g., around 9 Gyr). Following the erosion of light material, the long-term build up of heat in the thermochemical pile (from 7 to 9 Gyr) manifests a less dense region localized towards the top of the pile. By 9 Gyr, the density anomaly plot is dominated by an upwelling that extends to the base of the upper mantle. Following the impingement of the plume (from 9 to 11 Gyr), a fallout of dense blobs of primordial material are circulated about the mid-lower mantle. Compared with cases with lesser depth- dependence, the effect of composition dependence appears to have a greater influence on thermal instability (see cases #4 and #5 in Figure S11 compared with cases #16 and #17 in Figure 8). A lesser depth- dependence implicitly makes temperature- dependence the dominant factor in heat exchange. Thus, the effect of composition will easily be overshadowed.

When only n is increased from 0.5 to 0.8 (case #18), the onset of instability occurs $\sim$ 5 Gyr sooner compared to the reference case. Because it is more temperature dependent, thermal conductivity is reduced, which makes the heat transfer between the piles and the ambient mantle poorer. From 5 to 7 Gyr, similarly to case #17, the piles' retention of heat results in a reduced density anomaly (relative to the bulk pile). The ejection of primordial material from the largest of the two reservoirs occurs at 6.6 Gyr. The fallout blobs of primordial material are circulated in the lower mantle but are mainly localized above the pile. After 9 Gyr, the smaller pile is pushed by downwelling currents, and by 11 Gyr the piles coalesce.
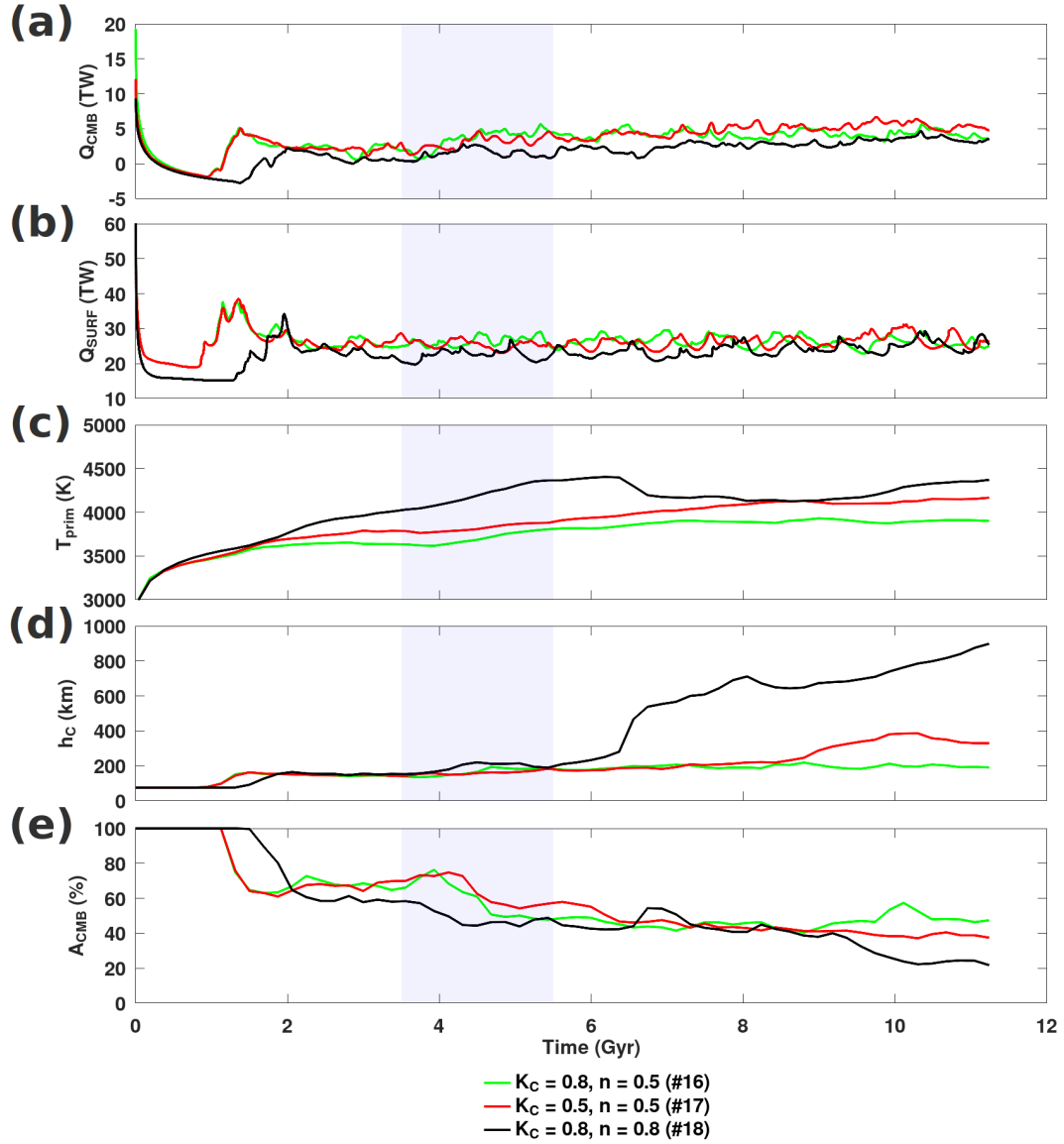
Figure 9. Evolution of cases corresponding to Figure 8. The quasi-stationary period centred about 4.5 Gyr is shaded in gray.

Examining the timeseries for the cases presented, T_{prim} increased marginally due to composition- dependence and increased significantly with temperature dependence (see Figure 9). In general, T_{prim} increases when thermochemical reservoir conductivity is reduced i.e., temperature- dependence (and, to a lesser extent, composition dependence) is strong. Only until h_C had
390   increased (indicating that piles became unstable and started eroding) T_{prim} decreases (i.e., case #18). Temperature- dependence greatly amplifies T_{prim} and is the dominant effect over composition. The long-term evolution of reservoirs characterized by a marginal temperature increase may result in a stable arrangement of piles with increased topography with respect to the

initial layering (see Figure 6, #16), whereas, a substantial increase in temperature (i.e., exceeding approximately 500 K) may lead to the entrainment of piles (see Figure 8, #18). Between these two cases, the onset of instability differs by approximately 4.5 Gyr. The differences in system's conductivity fields (profiles and bottom-to-top conductivity ratios) clarify these observations.

The distribution of light material ($C < 0.02$) is scattered about the lower mantle and may be ejected in small amounts into the upper mantle. An initial negative density anomaly is established compared with the mean mantle density (which is dominated by cold downwelling structures). When the thermochemical reservoirs finally become unstable, material with C between 0.02 and 0.90 is rapidly lifted away from the piles. This material dominates the mean density profile and produces a positive anomaly. The onset of light erosion precedes the onset of instability and the period between light and heavy erosion is reduced when the mean conductivity gradient is reduced (e.g., dotted and dot-dashed curves in Figure 8, and Figure S14. Interestingly, the radial conductivity profile obtained by models #16 and #17 lead to average CMB conductivity (and lower mantle conductivities) within values estimated from mineral physics (i.e., between 3 and 10 $\mathrm{Wm}^{-1}\mathrm{K}^{-1}$) (Hsieh et al., 2018; Deschamps & Hsieh, 2019; Geballe et al., 2020) (see Figure S14). However, the mean conductivity values in the lower mantle obtained by case #18 span the lower end of current estimates.

4   Discussion

The evolution of thermochemical reservoirs depends on their temperature and the mean bottom conductivity. The value of bottom conductivity results mainly from the competing thermal and pressure effects. Considering purely depth-dependent conductivity models, a greater lower mantle conductivity stabilizes thermochemical reservoirs by mitigating any (additional) thermal buoyancy imparted by internal heat sources. When temperature- dependence (and, to a lesser extent, composition- dependence) is considered, the conductivity of reservoirs is reduced with respect to the surrounding mantle. If depth- dependence is insufficient to compensate for this conductivity reduction, a positive feedback loop forms whereby a poorly conducting pile cannot evacuate heat, becomes hotter, and further reduces its conductivity. The imparted thermal buoyancy destabilizes the reservoirs and influences CMB coverage configuration, erosion rate, and the onset of entrainment. The effect of composition-dependence is secondary to the thermal effect and quickens the onset of instability (e.g., by approximately 2 Gyr, comparing cases #16 and #17; Figure 8). Moreover, the positive feedback loop persists over a prolonged period for conductivity models with greater depth- dependence (e.g., by approximately 4 Gyr, comparing cases #S6 and #17).

Our models are consistent with the 2-pile configuration found in lower resolution tomographic models. Of our simulations that attain a 2-pile configuration at approximately 4.5 Gyr, when $n = 0.5$ (lower temperature- dependent conductivity), we find that the conductivity fields suggest a pyrolytic lower mantle conductivity between 8 and 10 $\mathrm{Wm}^{-1}\mathrm{K}^{-1}$ and pile conductivity between 2 and 8 $\mathrm{Wm}^{-1}\mathrm{K}^{-1}$. When $n = 0.8$ (greater temperature- dependent conductivity), we find that the conductivity fields suggest a pyrolytic lower mantle conductivity approximately 5 $\mathrm{Wm}^{-1}\mathrm{K}^{-1}$ and pile conductivity between 2 and 4 $\mathrm{Wm}^{-1}\mathrm{K}^{-1}$. These simulations suggest that a conductivity ratio greater than 1.5 and not much greater than 2 can match estimates of lowermost mantle conductivity. Furthermore, we find that in combination with temperature- dependence, the depth- dependence

we propose K_{DH}, as well as linear profiles with $K_D = 5$ and 10, produce conductivity values between the upper and lower bounds of measurements made by Geballe et al. (2020). The values of h_C and A_{CMB} are overall consistent with observations pointing to mostly continuous LLSVPs (as seen, for instance in Houser et al. (2008) seismic tomography models), but somehow disagree with the bundle models proposed by Davaille & Romanowicz (2020) on the basis of full waveform tomography (French & Romanowicz, 2014). For instance, the maximum height of our piles is approximately 500 km, which is 300 km larger than the estimates of dense basal layer in high-resolution tomographic models (Davaille & Romanowicz, 2020) and the CMB coverage we find is greater than 30%. From our findings, we suggest that increasing the temperature dependence to an intermediate value between 0.5 and 0.8 could allow piles to attain less CMB coverage and more height; which, may help piles attain plume-like morphologies in addition to dense layering. Alternatively, lower buoyancy ratio and/or viscosity parameters may also lead to bundle-like structures (Deschamps et al., 2018).

Variations in the physical properties of thermochemical reservoirs, most notably the buoyancy ratio and enrichment in HPEs, have a strong influence on the long-term evolution of these reservoirs. Constraints on these properties are still being determined and subjects of ongoing research. Given the scope of this study, the effect of heterogeneous thermal conductivity on pile stability is difficult to differentiate from variable conditions that affect piles' chemical and thermal buoyancy. For example, greater composition- dependence for conductivity is related to pile's enrichment in iron and thus implies density increase requiring an increase in buoyancy ratio. In contrast, amount of enrichment in HPEs will directly influence the thermal buoyancy and destabilize piles in the long-term. Furthermore, we do not consider a decaying rate of internal heating. Assuming a mean 3 Gyr half life, internal heating rate should be reduced by almost an order of magnitude by the end of the simulation period we consider. It may be possible that the stronger influence of thermal buoyancy is limited to earlier periods of maximum heat input. The influence of these parameters in conjunction with the moderate heterogeneous conductivity profile we propose (i.e., case #16) should be examined in further detail.

The core-mantle boundary temperature may also be an important factor in the stability and evolution of thermochemical reservoirs when a heterogeneous conductivity is considered. In our study, the reference state imposes a CMB temperature ($T_{CMB} = 3440$ K) that is on the lower end of current estimates (for a recent review see Frost et al. (2022)). Several studies, including Boehler (2000); Price et al. (2004) and Kawai & Tsuchiya (2009) suggest greater temperatures, in excess of 3750 K and up to 4000 K, are possible. For the constant system heating conditions we consider, a greater CMB temperature implies that the mean temperatures in the lowermost mantle will also be increased, resulting in a lower thermal conductivity in that region and within the piles. In addition, higher thermal gradients at the base of the mantle will result in an increase in mean CMB heat flow. Thus, at very high CMB temperatures piles may become unstable. However, stable piles (under hotter conditions) can be accommodated by considering a lower n or a greater depth- dependent conductivity, or by other physical parameters (e.g., temperature- dependence of viscosity, or buoyancy ratio). Therefore, conclusions drawn from our results should be unchanged. Because a cooling bottom boundary is not considered, it is possible that piles evolving with our CMB temperature (or in hotter systems) could become more stable as the mantle cools and the mean lowermost mantle conductivity (and potentially the CMB heat flow) rises. However, examining evolving system heating conditions is out of the scope of our study.

Alternative formulations of the lattice conductivity exist in the literature featuring temperature and density dependences

(e.g., Manthilake et al., 2011; Okuda et al., 2017). Furthermore, measurements of the temperature dependent exponent for lower mantle materials may take on values that are less than 0.5 (i.e., between 0.2 and 0.47). For the lattice conductivity we consider, a lower exponent (lesser temperature dependence) will promote stability in piles. In addition, the radiative component of conductivity is much less than the lattice component for temperatures less than the CMB temperature (e.g., Dubuffet et al., 1999). It may be possible that the piles' temperature increases we observe could curb the conductivity reduction due to the lattice component. We do not rule out these possibilities but propose that different conductivity formulations are subjects for future studies.

5 Conclusions

In this study, we investigate the influence of variations in thermal conductivity on thermochemical convection, and find that a heterogeneous conductivity strongly influences the long-term evolution of thermochemical reservoirs. The combined influences of temperature- and depth- variations determines the mean conductivity ratio from bottom-to-top. In the calculations we present, for the mean conductivity profile to be comparable to the conductivity often assumed in numerical models, the depth- dependent ratio must be at least 9 times the surface conductivity. The composition- dependence for conductivity only plays a minor role that augments and behaves similarly to a small conductivity reduction due to temperature. Nevertheless, this effect may be amplified when depth- dependence is increased. For the cases we examine, when the mean conductivity in the lowermost mantle is much greater than the surface conductivity, large reservoirs can be maintained until the end of the simulation.

Code and data availability. The numerical code is available by reasonable request to Paul James Tackley. The data corresponding to the numerical simulations are too large to be stored online, but they can be requested from the corresponding authors as well as the input files used to run the simulations.

Author contributions. Joshua M. Guerrero: contributed to the study design, formal analysis, visualization, and writing - original draft preparation. Frédéric Deschamps: contributed to the study design, investigation, visualization, writing - review & editing. Yang Li: contributed to writing - review & editing. Wen-Pin Hsieh: contributed to consultation on the thermal conductivity model and writing - review & editing. Paul J. Tackley: contributed to software by designing the 3D thermochemical convection code and writing - review & editing. All authors collaborated and contributed intellectually to this paper.

Competing interests. The authors declare that they have no conflict of interest.

Acknowledgements. This study was funded by Ministry of Science and Technology, Taiwan (MoST) grant MOST 110-2116-M-001-025.

References

Ammann, M. W., Walker, A. M., Stackhouse, S., Wookey, J., Forte, A. M., Brodholt, J. P., & Dobson, D. P. 2014. Variation of thermal conductivity and heat flux at the Earth's core mantle boundary. Earth and Planetary Science Letters, 390, 175-185.

Boehler, R. 2000. High-pressure experiments and the phase diagram of lower mantle and core materials. Reviews of Geophysics, 38(2), 221-245.

Chang, Y. Y., Hsieh, W. P., Tan, E., & Chen, J. 2017. Hydration-reduced lattice thermal conductivity of olivine in Earth's upper mantle. Proceedings of the National academy of Sciences, 114(16), 4078-4081.

Citron, R. I., Lourenço, D. L., Wilson, A. J., Grima, A. G., Wipperfurth, S. A., Rudolph, M. L., ... & Montési, L. G. (2020). Effects of Heat-Producing Elements on the Stability of Deep Mantle Thermochemical Piles. Geochemistry, Geophysics, Geosystems, 21(4), e2019GC008895.

Davies, D. R., Goes, S., Davies, J. H., Schuberth, B. S. A., Bunge, H. P., & Ritsema, J. (2012). Reconciling dynamic and seismic models of Earth's lower mantle: The dominant role of thermal heterogeneity. Earth and Planetary Science Letters, 353, 253-269.

Dalton, D. A., Hsieh, W. P., Hohensee, G. T., Cahill, D. G., & Goncharov, A. F. 2013. Effect of mass disorder on the lattice thermal conductivity of MgO periclase under pressure. Scientific reports, 3(1), 1-5.

Davaille, A., & Romanowicz, B. 2020. Deflating the LLSVPs: bundles of mantle thermochemical plumes rather than thick stagnant "piles". Tectonics, 39(10), e2020TC006265.

Dekura, H., Tsuchiya, T., & Tsuchiya, J. 2013. Ab initio lattice thermal conductivity of MgSiO 3 perovskite as found in Earth's lower mantle. Physical Review Letters, 110(2), 025904.

Deschamps, F., & Hsieh, W. P. 2019. Lowermost mantle thermal conductivity constrained from experimental data and tomographic models. Geophysical Journal International, 219(Supplement 1), S115-S136.

Deschamps, F., Kaminski, E., & Tackley, P. J. 2011. A deep mantle origin for the primitive signature of ocean island basalt. Nature Geoscience, 4(12), 879-882.

Deschamps, F., Li, Y., & Tackley, P. J. 2015. Large-scale thermo-chemical structure of the deep mantle: observations and models. In The Earth's heterogeneous mantle (pp. 479-515). Springer, Cham.

Deschamps, F., Rogister, Y., & Tackley, P. J. 2018. Constraints on core-mantle boundary topography from models of thermal and thermo-chemical convection. Geophysical Journal International, 212(1), 164-188.

Dubuffet, F., & Yuen, D. A. 2000. A thick pipe-like heat-transfer mechanism in the mantle: Nonlinear coupling between 3-D convection and variable thermal conductivity. Geophysical research letters, 27(1), 17-20.

Dubuffet, F., Yuen, D. A., & Rabinowicz, M. 1999. Effects of a realistic mantle thermal conductivity on the patterns of 3-D convection. Earth and Planetary Science Letters, 171(3), 401-409.

Dubuffet, F., Yuen, D. A., & Yanagawa, T. 2000. Feedback effects of variable thermal conductivity on the cold downwellings in high Rayleigh number convection. Geophysical Research Letters, 27(18), 2981-2984.

French, S. W., & Romanowicz, B. A. 2014. Whole-mantle radially anisotropic shear velocity structure from spectral-element waveform tomography. Geophysical Journal International, 199(3), 1303-1327.

Frost, D. A., Avery, M. S., Buffett, B. A., Chidester, B. A., Deng, J., Dorfman, S. M., ... & Martin, J. F. (2022). Multidisciplinary Constraints on the Thermal-Chemical Boundary Between Earth's Core and Mantle. Geochemistry, Geophysics, Geosystems, 23(3), e2021GC009764.

Garnero, E. J., McNamara, A. K., & Shim, S. H. 2016. Continent-sized anomalous zones with low seismic velocity at the base of Earth's mantle. Nature Geoscience, 9(7), 481-489.

Geballe, Z. M., Sime, N., Badro, J., van Keken, P. E., & Goncharov, A. F. 2020. Thermal conductivity near the bottom of the Earth's lower mantle: Measurements of pyrolite up to 120 GPa and 2500 K. Earth and Planetary Science Letters, 536, 116161.

Goncharov, A. F., Lobanov, S. S., Tan, X., Hohensee, G. T., Cahill, D. G., Lin, J. F., ... & Tomioka, N. 2015. Experimental study of thermal conductivity at high pressures: Implications for the deep Earth's interior. Physics of the Earth and Planetary Interiors, 247, 11-16.

Gülcher, A. J., Gebhardt, D. J., Ballmer, M. D., & Tackley, P. J. 2020. Variable dynamic styles of primordial heterogeneity preservation in the Earth's lower mantle. Earth and Planetary Science Letters, 536, 116160.

Haigis, V., Salanne, M., & Jahn, S. 2012. Thermal conductivity of MgO, MgSiO3 perovskite and post-perovskite in the Earth's deep mantle. Earth and Planetary Science Letters, 355, 102-108.

Hernlund, J. W., & Tackley, P. J. 2008. Modeling mantle convection in the spherical annulus. Physics of the Earth and Planetary Interiors, 171(1-4), 48-54.

Heyn, B. H., Conrad, C. P., & Trønnes, R. G. 2020. How thermochemical piles can (periodically) generate plumes at their edges. Journal of Geophysical Research: Solid Earth, 125(6), e2019JB018726.

Hirose, K., Fei, Y., Ma, Y., & Mao, H. K. 1999. The fate of subducted basaltic crust in the Earth's lower mantle. Nature, 397(6714), 53-56.

Hofmeister, A. M. 1999. Mantle values of thermal conductivity and the geotherm from phonon lifetimes. Science, 283(5408), 1699-1706.

Houser, C., Masters, G., Shearer, P., & Laske, G. 2008. Shear and compressional velocity models of the mantle from cluster analysis of long-period waveforms. Geophysical Journal International, 174(1), 195-212.

Hsieh, W. P., Deschamps, F., Okuchi, T., & Lin, J. F. 2017. Reduced lattice thermal conductivity of Fe-bearing bridgmanite in Earth's deep mantle. Journal of Geophysical Research: Solid Earth, 122(7), 4900-4917.

Hsieh, W. P., Deschamps, F., Okuchi, T., & Lin, J. F. 2018. Effects of iron on the lattice thermal conductivity of Earth's deep mantle and implications for mantle dynamics. Proceedings of the National Academy of Sciences, 115(16), 4099-4104.

Jaupart, C., Labrosse, S. & Mareschal, J. In Treatise on Geophysics. Volume 7: Mantle Dynamics 1st edn (ed. Bercovici, D.) 253–303 (Elsevier, 2007).

Kanamori, H., Fujii, N., & Mizutani, H. 1968. Thermal diffusivity measurement of rock-forming minerals from 300 to 1100 K. Journal of geophysical research, 73(2), 595-605.

Katsura, T. 1997. Thermal diffusivity of periclase at high temperatures and high pressures. Physics of the earth and planetary interiors, 101(1-2), 73-77.

Katsura, T. 2022. A revised adiabatic temperature profile for the mantle. Journal of Geophysical Research: Solid Earth, 127(2), e2021JB023562.

Kawai, K., & Tsuchiya, T. 2009. Temperature profile in the lowermost mantle from seismological and mineral physics joint modeling. Proceedings of the National Academy of Sciences, 106(52), 22119-22123.

Klemens, P. G. 1960. Thermal resistance due to point defects at high temperatures. Physical review, 119(2), 507.

Labrosse, S., Hernlund, J. W., & Coltice, N. 2007. A crystallizing dense magma ocean at the base of the Earth's mantle. Nature, 450(7171), 866-869.

Lee, C. T. A., Luffi, P., Höink, T., Li, J., Dasgupta, R., & Hernlund, J. 2010. Upside-down differentiation and generation of a 'primordial' lower mantle. Nature, 463(7283), 930-933.

Li, Y., Deschamps, F., & Tackley, P. J. 2014. The stability and structure of primordial reservoirs in the lower mantle: insights from models of thermochemical convection in three-dimensional spherical geometry. Geophysical Journal International, 199(2), 914-930.

Li, Y., Deschamps, F., & Tackley, P. J. 2015. Effects of the post-perovskite phase transition properties on the stability and structure of primordial reservoirs in the lower mantle of the Earth. Earth and Planetary Science Letters, 432, 1-12.

Li, Y., Vilella, K., Deschamps, F., Zhao, L., & J. Tackley, P. 2018. Effects of iron spin transition on the structure and stability of large primordial reservoirs in Earth's lower mantle. Geophysical Research Letters, 45(12), 5918-5928.

Li, Y., Deschamps, F., Yang, J., Chen, L., Zhao, L., & Tackley, P. J. 2019. Effects of the Compositional Viscosity Ratio on the Long-Term Evolution of Thermochemical Reservoirs in the Deep Mantle. Geophysical Research Letters, 46(16), 9591-9601.

Li, Y., Deschamps, F., Shi, Z., Guerrero J. M., Hsieh, W. P., & Tackley, P. J. 2022 Influence of composition-dependent thermal conductivity on the long-term evolution of primordial reservoirs in Earth's lower mantle. Earth Planets Space 74, 46 (2022). https://doi.org/10.1186/s40623-022-01608-3

Manthilake, G. M., de Koker, N., Frost, D. J., & McCammon, C. A. 2011. Lattice thermal conductivity of lower mantle minerals and heat flux from Earth's core. Proceedings of the National Academy of Sciences, 108(44), 17901-17904.

Mosca, I., Cobden, L., Deuss, A., Ritsema, J., & Trampert, J. 2012. Seismic and mineralogical structures of the lower mantle from probabilistic tomography. Journal of Geophysical Research: Solid Earth, 117(B6).

Nakagawa, T., Tackley, P. J., Deschamps, F., & Connolly, J. A. 2009. Incorporating self-consistently calculated mineral physics into thermochemical mantle convection simulations in a 3-D spherical shell and its influence on seismic anomalies in Earth's mantle. Geochemistry, Geophysics, Geosystems, 10(3).

Ohta, K., Yagi, T., Taketoshi, N., Hirose, K., Komabayashi, T., Baba, T., ... & Hernlund, J. 2012. Lattice thermal conductivity of MgSiO3 perovskite and post-perovskite at the core-mantle boundary. Earth and Planetary Science Letters, 349, 109-115.

Okuda, Y., Ohta, K., Yagi, T., Sinmyo, R., Wakamatsu, T., Hirose, K., & Ohishi, Y. 2017. The effect of iron and aluminum incorporation on lattice thermal conductivity of bridgmanite at the Earth's lower mantle. Earth and Planetary Science Letters, 474, 25-31.

Price, G. D., Alfè, D., Vočadlo, L., & Gillan, M. J. 2004. The Earth's core: an approach from first principles. American Geophysical Union.

Stackhouse, S., Stixrude, L., & Karki, B. B. 2015. First-principles calculations of the lattice thermal conductivity of the lower mantle. Earth and Planetary Science Letters, 427, 11-17.

Tackley, P. J. 1998. Three-dimensional simulations of mantle convection with a thermo-chemical basal boundary layer: D. The Core-Mantle Boundary Region, Geodyn. Ser, 28, 231-253.

Tackley, P. J. 2008. Modelling compressible mantle convection with large viscosity contrasts in a three-dimensional spherical shell using the yin-yang grid. Physics of the Earth and Planetary Interiors, 171(1), 7-18.

Tan, E., Leng, W., Zhong, S., & Gurnis, M. 2011. On the location of plumes and lateral movement of thermochemical structures with high bulk modulus in the 3-D compressible mantle. Geochemistry, Geophysics, Geosystems, 12(7).

Tang, X., Ntam, M. C., Dong, J., Rainey, E. S., & Kavner, A. 2014. The thermal conductivity of Earth's lower mantle. Geophysical Research Letters, 41(8), 2746-2752.

Tosi, N., Yuen, D. A., de Koker, N., & Wentzcovitch, R. M. 2013. Mantle dynamics with pressure-and temperature-dependent thermal expansivity and conductivity. Physics of the Earth and Planetary Interiors, 217, 48-58.

Trampert, J., Deschamps, F., Resovsky, J., & Yuen, D. 2004. Probabilistic tomography maps chemical heterogeneities throughout the lower mantle. Science, 306(5697), 853-856.

Xu, Y., Shankland, T. J., Linhardt, S., Rubie, D. C., Langenhorst, F., & Klasinski, K. 2004. Thermal diffusivity and conductivity of olivine, wadsleyite and ringwoodite to 20 GPa and 1373 K. Physics of the Earth and Planetary Interiors, 143, 321-336.

600 Yamazaki, D., & Karato, S. I. 2001. Some mineral physics constraints on the rheology and geothermal structure of Earth's lower mantle. American Mineralogist, 86(4), 385-391.

Yanagawa, T. K., Nakada, M., & Yuen, D. A. 2005. Influence of lattice thermal conductivity on thermal convection with strongly temperature-dependent viscosity. Earth, planets and space, 57(1), 15-28.

Zhang, Y., Yoshino, T., Yoneda, A., & Osako, M. 2019. Effect of iron content on thermal conductivity of olivine with implications for cooling
605 history of rocky planets. Earth and Planetary Science Letters, 519, 109-119.